

## MATERIALS SCIENCE

Unraveling the atomic structure, ripening behavior, and electronic structure of supported Au<sub>20</sub> clusters

Zhe Li<sup>1\*</sup>, Hsin-Yi Tiffany Chen<sup>2</sup>, Koen Schouteden<sup>3</sup>, Thomas Picot<sup>3</sup>,  
Ting-Wei Liao<sup>3</sup>, Aleksandr Seliverstov<sup>3</sup>, Chris Van Haesendonck<sup>3</sup>,  
Gianfranco Pacchioni<sup>4</sup>, Ewald Janssens<sup>3</sup>, Peter Lievens<sup>3\*</sup>

The free-standing Au<sub>20</sub> cluster has a unique tetrahedral shape and a large HOMO-LUMO (highest occupied molecular orbital–lowest unoccupied molecular orbital) gap of around 1.8 electron volts. The “magic” Au<sub>20</sub> has been intensively used as a model system for understanding the catalytic and optical properties of gold nanoclusters. However, direct real-space ground-state characterization at the atomic scale is still lacking, and obtaining fundamental information about the corresponding structural, electronic, and dynamical properties, is challenging. Here, using cluster-beam deposition and low-temperature scanning tunneling microscopy, atom-resolved topographic images and electronic spectra of supported Au<sub>20</sub> clusters are obtained. We demonstrate that individual size-selected Au<sub>20</sub> on ultrathin NaCl films maintains its pyramidal structure and large HOMO-LUMO gap. At higher cluster coverages, we find sintering of the clusters via Smoluchowski ripening to Au<sub>20n</sub> agglomerates. The evolution of the electron density of states deduced from the spectra reveals gap reduction with increasing agglomerate size.

## INTRODUCTION

Few-atom gold clusters have attracted intensive research interest due to their atypical chemical and electronic properties and corresponding potential applications in catalysis (1–5) and optics (6, 7). Particular attention has been focused on understanding size dependences, requiring controllable synthesis and characterization of well-defined clusters with atomic precision (8, 9). Among all ligand-free clusters, Au<sub>20</sub> was investigated intensively, both with theory and experiment, because of its high-symmetry tetrahedral structure and exceptionally large HOMO-LUMO (highest occupied molecular orbital–lowest unoccupied molecular orbital; henceforth referred to as HL) gap. Photoelectron spectroscopy (PES) experiments on isolated anionic Au<sub>20</sub><sup>−</sup> revealed that the neutral Au<sub>20</sub> cluster has an HL gap of 1.77 eV (10). Density functional theory (DFT) simulations showed that such a large gap could only be reproduced by a *T<sub>d</sub>* symmetry tetrahedral pyramid structure, which is obtained as the most stable geometry for Au<sub>20</sub> (10). The tetrahedral structure was later confirmed by a combination of infrared spectroscopy experiments and DFT calculations (11), and its high stability was rationalized by its closed electron shell structure (12, 13).

Most applications require clusters on a support, which is realized reliably with cluster-beam deposition of gas phase–produced clusters in an ultrahigh vacuum (UHV) environment. Although solution synthesis of ligand-protected Au<sub>20</sub> has also been proposed (14), proper ligands and synthetic conditions still need to be explored, and ligands notably affect the structure and electronic properties of a bare cluster (15). Ensembles of UHV-produced Au<sub>20</sub> exhibit interesting macroscopic properties such as high catalytic reactivity (16) and intense fluorescence (17); however, there are few studies at the single

cluster level. So far, real-space imaging of Au<sub>20</sub> was reported only in one scanning transmission electron microscopy (STEM) experiment of Au<sub>20</sub> deposited on amorphous carbon films (18). Because of the high energy of the STEM electron beam, Au<sub>20</sub> was observed to continuously fluctuate between different structural configurations. The imaged Au<sub>20</sub> had tetrahedral projections in 5% of the frames, while a disordered geometry was observed in most frames. The existence and stability of the tetrahedral structure on surfaces therefore remain under question.

Here, we use less invasive techniques, i.e., scanning tunneling microscopy (STM) and scanning tunneling spectroscopy (STS) to explore the structural and electronic properties of size-selected Au<sub>20</sub> clusters on ultrathin NaCl films. These techniques are recognized as powerful tools to investigate nanoclusters (19–22). STM topography images of individual Au<sub>20</sub> reveal the triangular symmetry of the pyramidal structure, while a large HL gap of about 2.0 eV is extracted from the STS data. On the basis of our experiments and DFT calculations, we confirm that both the predicted pyramidal structure and the theoretically described closed-shell electronic configuration of Au<sub>20</sub> are retained on NaCl surfaces. Furthermore, by deposition of a high coverage of Au<sub>20</sub> clusters, a discrete distribution of the agglomerated clusters is observed, which can be explained by the Smoluchowski ripening mechanism for the supported Au<sub>20</sub> clusters. This ripening provides us with the unique opportunity to demonstrate the evolution of the electronic properties with cluster size, i.e., the HL gap decreases as the Au<sub>20</sub> clusters assemble to form larger agglomerates.

## RESULTS

Mass-selected Au<sub>20</sub> cluster anions with very low coverage (see Materials and Methods) are deposited at room temperature onto ultrathin NaCl islands including two (2L), three (3L), four (4L), and five (5L) atomic layers (Fig. 1). As shown in Fig. 1A, most parts of the grown NaCl are 3L with a small fraction of 2L and 4L and very few 5L NaCl. Clusters are found on 3L and 4L NaCl and not on 2L NaCl, which is consistent with our previous findings (21) that the Au<sub>20</sub>

Copyright © 2020  
The Authors, some  
rights reserved;  
exclusive licensee  
American Association  
for the Advancement  
of Science. No claim to  
original U.S. Government  
Works. Distributed  
under a Creative  
Commons Attribution  
NonCommercial  
License 4.0 (CC BY-NC).

<sup>1</sup>State Key Laboratory on Tunable Laser Technology, Ministry of Industry and Information Technology Key Lab of Micro-Nano Optoelectronic Information System, School of Science, Harbin Institute of Technology, Shenzhen 518055, China. <sup>2</sup>Department of Engineering and System Science, National Tsing Hua University, Hsinchu 30013, Taiwan. <sup>3</sup>Quantum Solid-State Physics, Department of Physics and Astronomy, KU Leuven, BE-3001 Leuven, Belgium. <sup>4</sup>Dipartimento di Scienza dei Materiali, Università di Milano-Bicocca, I-20125 Milano, Italy.

\*Corresponding authors. Email: zhe.li@hit.edu.cn (Z.L.); peter.lievens@kuleuven.be (P.L.)

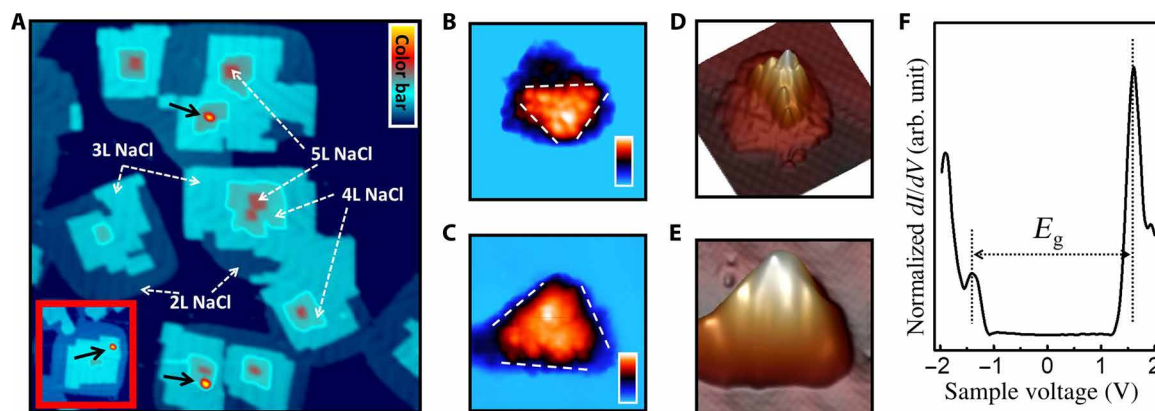


**Fig. 1. Evidence of the pyramidal  $\text{Au}_{20}$  clusters on ultrathin NaCl films.** (A) STM topography image (200 nm by 200 nm) of  $\text{Au}_{20}$  clusters on 3L and 4L NaCl islands ( $V = -2.0$  V,  $I = 0.02$  nA). Three  $\text{Au}_{20}$  clusters are indicated by the black arrows. The one in the inset (dimensions, 80 nm by 73 nm) is on top of a 3L NaCl film, while the two others are on top of 4L NaCl. (B and C) Triangular-shaped  $\text{Au}_{20}$  clusters with one atom on top, imaged with Cl-functionalized STM tips. Dimensions for both (B) and (C), 10 nm by 10 nm. (D and E) Three-dimensional views (with fast Fourier transform filtering) of the clusters in (B) and (C), respectively. (F) Normalized  $dI/dV$  [( $dI/dV$ )/( $I/V$ )] spectra taken on a  $\text{Au}_{20}$  cluster on 3L NaCl.  $E_g$  is the energy gap around the Fermi level.

penetrates through 2L NaCl, while it can stay on top of 3L and 4L NaCl. Using low coverages, only zero to four well-separated clusters can be observed in a 200 nm by 200 nm STM scanning area, without any indication of agglomeration of the  $\text{Au}_{20}$ . Because of the too high resistance of the 4L NaCl and the instability when scanning the individual  $\text{Au}_{20}$  on 4L NaCl, we focus on clusters on 3L NaCl in what follows. The STM-measured height for clusters on 3L NaCl is  $0.88 \pm 0.12$  nm, which compares well to the DFT-simulated height of  $0.94 \pm 0.01$  nm for a pyramidal  $\text{Au}_{20}$  on a 3L NaCl film (Fig. 2A). Using Cl-functionalized STM tips (23), the  $\text{Au}_{20}$  clusters were, in some cases, imaged as a triangular shape with one protruding atom. This is consistent with the theoretical picture of a pyramidal  $\text{Au}_{20}$  cluster atop a 3L NaCl film (see Fig. 2B). We note that for imaging a small three-dimensional  $\text{Au}_{20}$  cluster, tip convolution effects are almost impossible to avoid. Therefore, an ideal atomically sharp Cl-functionalized STM tip is necessary to obtain both atomic and geometrical resolution. We have attempted to get the atomic resolution for about eight clusters. The pyramidal shape was found with different Cl-functionalized STM tips for the two clusters shown in Fig. 1 (B and C). The corresponding three-dimensional views of these two clusters are shown in Fig. 1 (D and E, respectively). An additional cluster showing the feature of one protruded atom is illustrated in fig. S1, although the pyramidal feature is less pronounced. Atomic resolution was not realized for the other clusters due to the instability of the Cl-functionalized tips. Although the triangular shape and height distribution show that the deposited clusters maintain a pyramidal shape, the STM images in Fig. 1 (B and C) do not show perfect tetrahedral structures. The largest angle in Fig. 1B is around  $78^\circ$ , indicating a large distortion at least of 30% with respect to  $60^\circ$  for a perfect  $T_d$  symmetry tetrahedron. There can be two reasons for this. The first is related to the imaging technique. The tip convolution effect can distort the image. In addition, the Cl-functionalized tip is not stiff, which may also distort the STM images. Such an effect is well studied in the atomic imaging of single molecules when using a CO-functionalized atomic force microscopy tip (24). The second reason is related to intrinsic distortion of the supported  $\text{Au}_{20}$ . When the  $\text{Au}_{20}$  clusters with  $T_d$  symmetry land on the square lattice of NaCl, the symmetry mismatch distorts the perfect tetrahedral structure of

$\text{Au}_{20}$ . We analyzed the symmetry information of three optimized structures of  $\text{Au}_{20}$  on NaCl (see Fig. 2 and table S1) and found that the clusters are only slightly distorted from a perfect  $T_d$  symmetry tetrahedral structure, with the largest maximum deviation in atomic positions of  $0.45$  Å, a change that would not be easily resolved with the accuracy of the STM imaging technique. This indicates that the pyramidal  $\text{Au}_{20}$  is only slightly distorted from the tetrahedral structure and, consequently, that the distortion from the tetrahedral symmetry in Fig. 1 (B and C) is largely due to the tip convolution effect and/or the flexibility of Cl-functionalized STM tips.

Besides the topographic information, another fingerprint of the pyramidal  $\text{Au}_{20}$  is the much larger HL gap (around 1.8 eV), compared to the gap for other lower-energy  $\text{Au}_{20}$  isomers (below 0.5 eV theoretically) (10). We examined the electronic properties of the deposited clusters by performing STS measurements. Figure 1F shows a differential conductance ( $dI/dV$ ) spectrum taken on a  $\text{Au}_{20}$  cluster, which shows a large energy gap ( $E_g$ ) of 3.1 eV around the Fermi level. Since the cluster is electrically decoupled by the insulating NaCl films, a double-barrier tunnel junction (DBTJ) [tip cluster and cluster  $\text{Au}(111)$ ] is formed, which gives rise to single-electron tunneling effects. Therefore, the gap in the  $dI/dV$  spectrum reflects contributions from (i) the quantum HL gap ( $E_{\text{HL}}$ ) and (ii) the classical Coulomb charging energy ( $E_c$ ). The measured gap in  $dI/dV$  spectra ranges from 2.4 to 3.1 eV for seven clusters (see Fig. 1F and fig. S2). The observed gaps are larger than the HL gap (1.8 eV) of gas-phase  $\text{Au}_{20}$ , indicating that the supported  $\text{Au}_{20}$  has a large HL gap as well. Differences in the measured gap (see Fig. 1F and fig. S2) are attributed to the different tip apex conditions for each measurement, which changes the capacitor associated with tip and cluster, and, thus, the charging energy within the DBTJ model (25). Consequently, the observed gap ( $E_{\text{HL}} + E_c$ ) in  $dI/dV$  spectra is expected to differ to some extent in different measurements. The largest gap measured in  $dI/dV$  spectra is 3.1 eV, in which case, the tip is far from the cluster and, hence, the capacitance between tip and cluster ( $C_1$ ) can be considered to be much smaller than the capacitance between the cluster and  $\text{Au}(111)$  substrate ( $C_2$ ). In this limit, the measured gap is described as  $E_g = E_{\text{HL}} + E_c$ , where  $E_c = e^2/C_2$ . We estimate that  $E_c$  is  $1.1 \pm 0.1$  eV (see fig. S3). Then, the HL gap is  $E_g - E_c = 3.1 \text{ eV} - (1.1 \pm 0.1) \text{ eV} = (2.0 \pm 0.1) \text{ eV}$ .

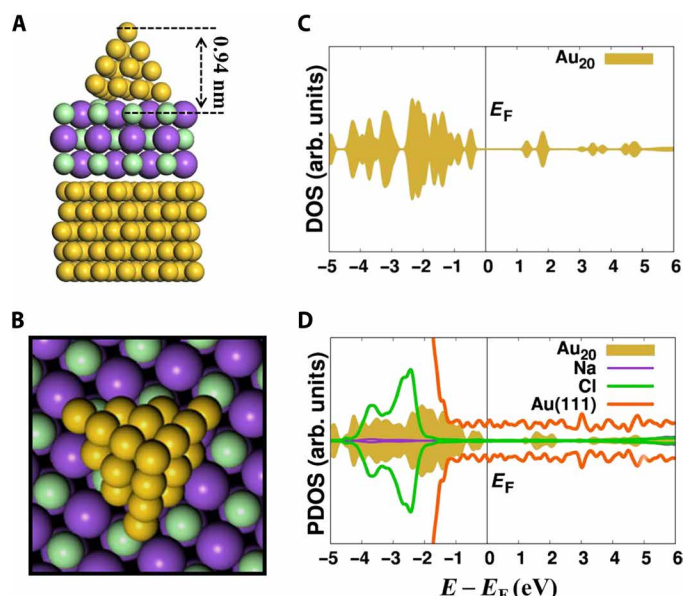


**Fig. 2. DFT simulation of the structural and electronic properties of a pyramidal  $\text{Au}_{20}$  cluster.** (A) Side view and (B) top view of the optimized structure of a  $\text{Au}_{20}$  cluster on 3L NaCl/Au(111). The theoretical STM measured height ( $0.94 \pm 0.01$  nm) for a  $\text{Au}_{20}$  cluster on NaCl is the vertical distance between the top atom of  $\text{Au}_{20}$  and the NaCl surface, as indicated by the dashed lines in (A). (C) DOS curve of a free  $\text{Au}_{20}$  cluster. (D) Projected DOS (PDOS) curve for a  $\text{Au}_{20}$  cluster supported on 3L NaCl/Au(111).

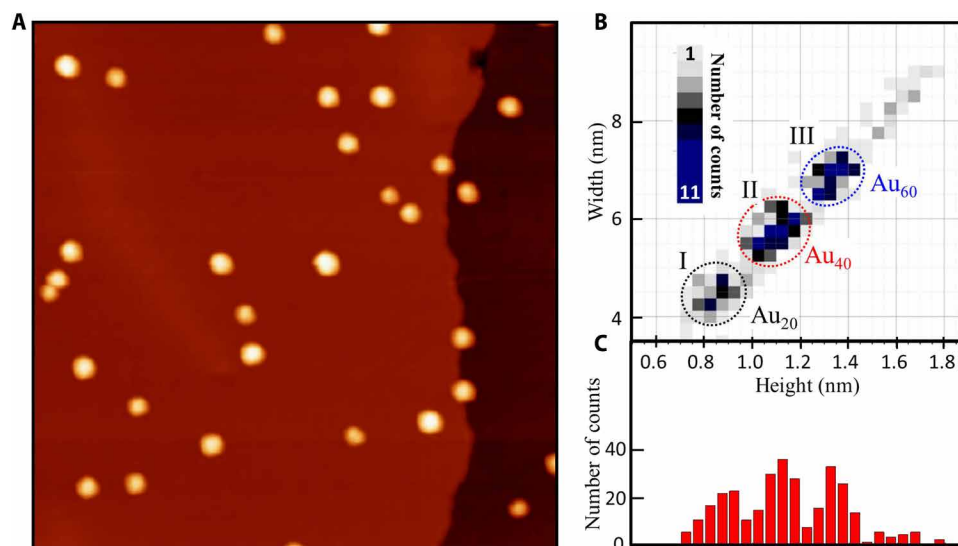
We performed DFT calculations to compute the HL gap of the free  $\text{Au}_{20}$  and that of the supported  $\text{Au}_{20}$  on 3L NaCl. Figure 2C illustrates the simulated density of states (DOS) curve for the gas-phase tetrahedral  $\text{Au}_{20}$ , which has an HL gap of 1.78 eV, consistent with previous experimental and theoretical results (10). When it is on top of 3L NaCl/Au(111), with increasing distortion, the HL gap (Fig. 2D) decreases from 1.73 to 1.51 eV (see table S1), which is comparable with the HL gap (2.0 eV) extracted from the experimental  $dI/dV$  measurements as discussed above. Our simulations indicate that small distortions can result in some changes in HL gap but do not induce a significant change. Other  $\text{Au}_{20}$  isomers beyond tetrahedrons are not considered in our calculations, since their gas-phase HL gaps (10) are much smaller than 2.0 eV and hence would fail to reproduce our experimental observations. For highly distorted pyramidal structures in gas phase, the HL gap was also reported to be much smaller. For example, Wang *et al.* (26) reported that a large gap of 1.433 eV is found in the  $T_d$  symmetry structure of  $\text{Au}_{20}$  and a much smaller gap of 0.688 eV in a compact  $C_s$  symmetry structure. Fernández *et al.* (27) analyzed four  $\text{Au}_{20}$  isomers, the  $T_d$  structure, and three low-symmetry structures and found that the gap drops from 1.83 eV for  $T_d$  symmetry to 0.93 eV for a  $C_1$  symmetry amorphous structure, which is only slightly less stable. The other structures have even smaller HL gaps. Therefore, a large bandgap like that experimentally observed here is consistent only with a tetrahedral-like, pyramidal structure.

To study cluster-cluster interactions, we deposit a higher coverage of  $\text{Au}_{20}$  clusters onto 3L NaCl/Au(111) (see the Supplementary Materials). Figure 3A shows the STM topography image of the deposited clusters. Around 30 clusters can be observed in a 100 nm by 100 nm STM scanning area. The observed clusters on the high-coverage 3L NaCl sample have different sizes that are either equal or

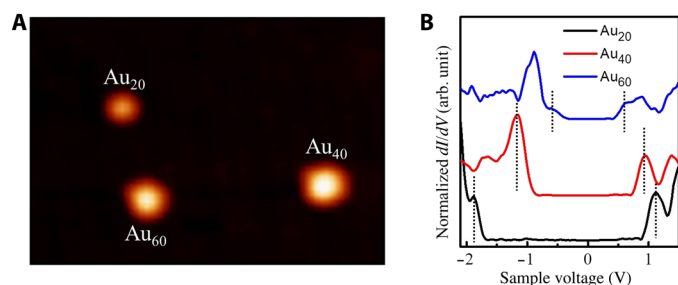
larger than the sizes of single  $\text{Au}_{20}$  clusters in the low-coverage sample. This can be explained by diffusion and agglomeration on the NaCl surface at room temperature. Cluster agglomeration and growth are commonly ascribed to two mechanisms, Ostwald ripening and Smoluchowski ripening. For Ostwald ripening, larger clusters grow at the expense of smaller clusters, from which single atoms detach and diffuse into a neighboring cluster. For Smoluchowski ripening, larger particles are formed by the migration and agglomeration of entire clusters. A straightforward feature to distinguish Ostwald and Smoluchowski ripening is that, for the former, the distribution of the cluster size is broadened and continuous, while for the latter, the size is discretely distributed (28). We have carefully analyzed the height and the corresponding width of each cluster resulting from one or several  $\text{Au}_{20}$  clusters, as inferred from STM height profiles (21). The size distribution of more than 300 clusters is plotted in Fig. 3 (B and C). Although the clusters exhibit a broad range of heights, as illustrated in Fig. 3C, three discrete groups of heights (centered at around 0.85, 1.10, and 1.33 nm) can be observed. This discrete size distribution can be more clearly observed in Fig. 3B, where the abundance of the clusters is plotted in a population graph as function of both height and width, showing a clear correlation between the height and the width and the presence of three groups of characteristic sizes; a fourth group also is discernable. These are indicated by the dotted circles and constitute direct evidence that the agglomeration of the supported  $\text{Au}_{20}$  clusters follows the Smoluchowski ripening mechanism. The first group with a height centered at around 0.85 nm is consistent with the height (around 0.88 nm) of the individual  $\text{Au}_{20}$  in the low-coverage experiments described above. We assign the clusters in the first group to be  $\text{Au}_{20}$ . Clusters in groups II and III with heights centered at around 1.10 and 1.33 nm are attributed to  $\text{Au}_{40}$  and  $\text{Au}_{60}$ , respectively.

Figure 4A shows three clusters with heights of 0.85, 1.10, and 1.30 nm, which can be classified to  $\text{Au}_{20}$ ,  $\text{Au}_{40}$ , and  $\text{Au}_{60}$ , respectively. The corresponding  $dI/dV$  spectra, recorded using the same STM tip, are shown in Fig. 4B. As the  $\text{Au}_{20}$  coalesces into larger clusters, the gap in the  $dI/dV$  spectra decreases. For  $\text{Au}_{20}$ ,  $\text{Au}_{40}$ , and  $\text{Au}_{60}$ , we find gaps of 3.0, 2.0, and 1.2 eV, respectively. As discussed above, the gap is the sum of the HL gap and the charging energy. To obtain the charging energy for  $\text{Au}_{40}$  and  $\text{Au}_{60}$ , information of their three-dimensional morphology is required. High-resolution STM topography images of a  $\text{Au}_{40}$  cluster and a  $\text{Au}_{60}$  cluster (see fig. S5) exhibit shapes with a circular footprint. Therefore, we infer that the most plausible geometries of the cluster agglomerates are sphere or hemisphere like. In the spherical-shape or hemispherical-shape approximation, the number of the atoms in a cluster can be estimated as  $N_s = \left(\frac{h}{r}\right)^3$  or  $N_h = \frac{1}{2}\left(\frac{h}{r}\right)^3$ , respectively, where  $h$  and  $r$  represent the cluster height and the radius of a single Au atom, respectively. Using the Wigner-Seitz radius for a gold atom ( $r = 0.159$  nm), in the spherical approximation, clusters with heights of 1.10 and 1.30 nm contain 41 and 68 atoms, corresponding to  $\text{Au}_{40}$  and  $\text{Au}_{60}$ , respectively. In the hemispherical approximation, the estimated number of atoms, 166 and 273, is much larger than in  $\text{Au}_{40}$  and  $\text{Au}_{60}$ , respectively. Therefore, we can conclude that the geometry of  $\text{Au}_{40}$  and  $\text{Au}_{60}$  is spherical like, rather than hemispherical like. Again, within the approximation of  $C_1 \ll C_2$ , the charging energy for  $\text{Au}_{40}$  and  $\text{Au}_{60}$  is estimated to be  $1.6 \pm 0.1$  eV and  $1.0 \pm 0.1$  eV, respectively (see fig. S4). Then, we extract the HL gap for  $\text{Au}_{40}$  being  $0.4 \pm 0.1$  eV and that for  $\text{Au}_{60}$  being  $0.2 \pm 0.1$  eV. This is consistent with the HL gap evolution observed in previous photoelectron experiments on gas-phase gold clusters,





**Fig. 3. Smoluchowski ripening of Au<sub>20</sub> clusters on ultrathin NaCl film.** (A) STM topography image of high-coverage Au<sub>20</sub> clusters on 3L NaCl/Au(111) (size, 100 nm by 100 nm;  $V = 1.5$  V,  $I = 0.05$  nA), using a normal STM metal tip. (B) Size distribution of more than 300 Au<sub>20n</sub> ( $n = 1, 2, \dots$ ) clusters on 3L NaCl/Au(111), where the counted number of clusters is plotted as function of their height and width. (C) Histogram of the height (with respect to the surrounding NaCl surface) distribution of clusters on 3L NaCl/Au(111). Note that (B) and (C) share the same horizontal axis.



**Fig. 4. Electronic properties of Au<sub>20</sub>, Au<sub>40</sub>, and Au<sub>60</sub>.** (A) STM topography image (size, 46 nm by 32 nm;  $V = 1.5$  V,  $I = 0.05$  nA) of three clusters (Au<sub>20</sub>, Au<sub>40</sub>, and Au<sub>60</sub>) on 3L NaCl/Au(111) with heights of 0.85, 1.1, and 1.3 nm, respectively, using a normal STM metal tip. (B) The corresponding  $dI/dV$  spectra of the three clusters in (A), using the same STM tip.

where the HL gap is closing from Au<sub>20</sub> to Au<sub>40</sub> and Au<sub>60</sub> clusters (29). Note that both larger sizes do not correspond to electronic shell closures for gold clusters (15). The structural and electronic properties of Au<sub>40</sub> and Au<sub>60</sub> have been previously investigated in the gas phase. For Au<sub>40</sub>, a putative global minimum was found to be a twisted pyramid structure with a sizable HL gap of 0.69 eV by DFT-based calculations (30). For Au<sub>60</sub>, combining PES experiments and DFT simulations (31), it was reported that Au<sub>60</sub> cluster are formed by simply adding two additional atoms to the surface of the parent Au<sub>58</sub> structure, where Au<sub>58</sub> was found to be nearly spherical with a large HL gap of 0.65 eV. The HL gap of Au<sub>60</sub> is around 0.2 eV derived from the experimental PES data (31). The derived HL gap of  $0.4 \pm 0.1$  eV ( $0.2 \pm 0.1$  eV) for the supported Au<sub>40</sub> (Au<sub>60</sub>) agglomerates on NaCl in our present work is comparable to that of 0.69 eV (0.2 eV) for the gas-phase Au<sub>40</sub> (Au<sub>60</sub>). Note that the HL gap deduced from PES is a (good) proxy for the neutral, assuming that the anion and the neutral have the same structure.

It actually gives the energy difference between the two highest occupied states of the anion. However, since it is not possible to probe the inner atoms using STM, the precise atomic structures of the supported Au<sub>40</sub> and Au<sub>60</sub> on NaCl were not identified in our study.

## DISCUSSION

In summary, combining the STM topographic and spectroscopic information, we have presented strong evidence that an individual Au<sub>20</sub> cluster deposited on 3L NaCl/Au(111) preserves its gas-phase pyramidal structure with a large HL gap. We also find evidence for Smoluchowski ripening of supported Au<sub>20</sub> on NaCl, forming Au<sub>20n</sub> ( $n = 1, 2, \dots$ ) clusters. The evolution of the HL gap as a function of the cluster size is revealed at the single cluster level. Our work demonstrates a generally applicable routine to study the intrinsic properties of well-defined clusters, as well as their sintering mechanism on surfaces. Detailed knowledge and understanding of morphology, size distribution, and electronic structure of supported clusters are important to evaluate their catalytic and optical performances and, hence, highly relevant to advancing the design of cluster-based catalysis and optical devices.

## MATERIALS AND METHODS

### Preparation of NaCl/Au(111) substrate

NaCl layers were grown on a Au(111) substrate using vapor deposition at 800 K in the preparation chamber of an STM setup (Oxford Instruments Omicron NanoScience) under UHV conditions. If the sample was left at room temperature during growth of the salt layers, then 2L and a small fraction of 3L NaCl(100) islands coexist on Au(111). By annealing the sample up to about 470 K for several minutes, most NaCl becomes 3L with small patches of 2L, 4L, and 5L NaCl.

## Cluster-beam deposition of mass-selected Au<sub>20</sub>

Au<sub>20</sub> cluster ions were produced in a home-built magnetron sputtering setup and size-selected by a quadrupole mass filter. The sputter source operates in continuous mode and produces a large fraction of charged clusters (32). The charged clusters were transferred and bended by ion guides and a quadrupole ion bender, respectively, and then entered a high-resolution radio-frequency quadrupole mass filter, allowing precise mass selection. Last, the size-selected clusters were soft-landed on the NaCl/Au(111) substrate. For low-coverage deposition, the cluster flux of mass-selected Au<sub>20</sub> cations was around 30 pA, and the deposition time was 9 min, while for the high-coverage deposition, a flux of around 1 nA and deposition time of 15 min was used. The UHV deposition chamber has a base pressure of 10<sup>−9</sup> mbar.

## Sample transfer

The sample was transferred from and to the STM setup by means of a home-built UHV transport vessel (pressure in the 10<sup>−10</sup> mbar range) (33).

## STM measurements

All STM measurements were performed in UHV (10<sup>−11</sup> mbar) and at low temperature ( $T_{\text{sample}} \approx 4.5$  K). For normal metallic STM tips, we used mechanically cut PtIr (10% Ir) and polycrystalline W wires. The W tips were electrochemically etched and cleaned in situ by thermal treatment. The Cl-functionalized STM tips were prepared by picking up a Cl ion onto the normal metal tips upon contact with the NaCl surface (23). All voltages refer to the sample bias with respect to the STM tip. STS data were acquired with open feedback loop. Image processing was performed by Nanotec WSxM (34).

## DFT simulations

DFT calculations were performed using the generalized gradient approximation [the Perdew, Burke, and Ernzerhof exchange-correlation functional (35)] and the plane waves code Vienna Ab initio Simulation Package (36, 37). The interaction between the ions and the valence electrons was described by the projector augmented wave method (38). The NaCl(100) films on the Au(111) substrate were modeled by a coincidence structure, obtained by superposing a (4 × 4) NaCl(100) unit cells on a  $\begin{pmatrix} 1 & 3 \\ 3 & 1 \end{pmatrix}$  superstructure of the Au(111) surface (39, 40). The metal support was modeled by a five-layer slab, and 1.4 nm of empty space was included to avoid spurious interactions between the replicas of the slab model. The  $\Gamma$  point was used for the reciprocal space sampling. Grimme dispersion correction (DFT-D2) was included, and the associated C<sub>6</sub> parameters and van der Waals radii of Na were replaced by those of Ne, whose size was similar to that of Na<sup>+</sup> cation (21, 41).

## SUPPLEMENTARY MATERIALS

Supplementary material for this article is available at <http://advances.sciencemag.org/cgi/content/full/6/1/eaay4289/DC1>

Fig. S1. Additional (next to Fig. 1, B and C) STM topography image of a Au<sub>20</sub> cluster on 3L NaCl/Au(111), imaged with a Cl-functionalized tip.

Fig. S2. Series of  $dI/dV$  spectra recorded on different Au<sub>20</sub> clusters with different conditions of STM tip apex.

Fig. S3. Electrostatic model to estimate the capacitance of Au<sub>20</sub>/NaCl/Au(111) system.

Fig. S4. Electrostatic model to estimate the capacitance of Au<sub>40</sub>/NaCl/Au(111) and Au<sub>60</sub>/NaCl/Au(111) systems.

Fig. S5. High-resolution STM images for supported Au<sub>40</sub> and Au<sub>60</sub> clusters.

Table S1. The relationship between distortion and the HL gap for supported Au<sub>20</sub>. Reference (42)

## REFERENCES AND NOTES

1. A. Sanchez, S. Abbet, U. Heiz, W.-D. Schneider, H. Häkkinen, R. N. Barnett, U. Landman, When gold is not noble: Nanoscale gold catalysts. *J. Phys. Chem. A* **103**, 9573–9578 (1999).
2. R. Meyer, C. Lemire, S. K. Shaikhutdinov, H.-J. Freund, Surface chemistry of catalysis by gold. *Gold Bulletin* **37**, 72–124 (2004).
3. B. Yoon, H. Häkkinen, U. Landman, A. S. Wörz, J.-M. Antonietti, S. Abbet, K. Judai, U. Heiz, Charging effects on bonding and catalyzed oxidation of CO on Au<sub>8</sub> clusters on MgO. *Science* **307**, 403–407 (2005).
4. S. Lee, C. Fan, T. Wu, S. L. Anderson, CO oxidation on Au<sub>n</sub>/TiO<sub>2</sub> catalysts produced by size-selected cluster deposition. *J. Am. Chem. Soc.* **126**, 5682–5683 (2004).
5. A. Halder, L. A. Curtiss, A. Fortunelli, S. Vajda, Perspective: Size selected clusters for catalysis and electrochemistry. *J. Chem. Phys.* **148**, 110901 (2018).
6. R. Philip, P. Chantharasupawong, H. Qian, R. Jin, J. Thomas, Evolution of nonlinear optical properties: From gold atomic clusters to plasmonic nanocrystals. *Nano Lett.* **12**, 4661–4667 (2012).
7. S. Lecoultré, A. Rydlo, C. Félix, J. Buttet, S. Gilb, W. Harbich, UV–visible absorption of small gold clusters in neon: Au<sub>n</sub> ( $n = 1–5$  and  $7–9$ ). *J. Chem. Phys.* **134**, 074302 (2011).
8. R. Jin, Atomically precise metal nanoclusters: Stable sizes and optical properties. *Nanoscale* **7**, 1549–1565 (2015).
9. E. C. Tyo, S. Vajda, Catalysis by clusters with precise numbers of atoms. *Nat. Nanotech.* **10**, 577–588 (2015).
10. J. Li, X. Li, H.-J. Zhai, L.-S. Wang, Au<sub>20</sub>: A tetrahedral cluster. *Science* **299**, 864–867 (2003).
11. P. Gruene, D. M. Rayner, B. Redlich, A. F. G. van der Meer, J. T. Lyon, G. Meijer, A. Fielicke, Structures of neutral Au<sub>7</sub>, Au<sub>19</sub>, and Au<sub>20</sub> clusters in the gas phase. *Science* **321**, 674–676 (2008).
12. L. Cheng, X. Zhang, B. Jin, J. Yang, Superatom–atom super-bonding in metallic clusters: A new look to the mystery of an Au<sub>20</sub> pyramid. *Nanoscale* **6**, 12440–12444 (2014).
13. P. V. Nhat, N. T. Si, J. Leszczynski, M. T. Nguyen, Another look at structure of gold clusters Au<sub>n</sub> from perspective of phenomenological shell model. *Chem. Phys.* **493**, 140–148 (2017).
14. Q.-F. Zhang, X. Chen, L.-S. Wang, Toward solution syntheses of the tetrahedral Au<sub>20</sub> pyramid and atomically precise gold nanoclusters with uncoordinated sites. *Acc. Chem. Res.* **51**, 2159–2168 (2018).
15. H. Häkkinen, Electronic shell structures in bare and protected metal nanoclusters. *Adv. Phys. X* **1**, 467–491 (2016).
16. M. Arenz, U. Landman, U. Heiz, CO combustion on supported gold clusters. *Chem. Phys. Chem* **7**, 1871–1879 (2006).
17. C. Yu, W. Harbich, L. Sementa, L. Ghiringhelli, E. Aprà, M. Stener, A. Fortunelli, H. Brune, Intense fluorescence of Au<sub>20</sub>. *J. Chem. Phys.* **147**, 074301 (2017).
18. Z. W. Wang, R. E. Palmer, Direct atomic imaging and dynamical fluctuations of the tetrahedral Au<sub>20</sub> cluster. *Nanoscale* **4**, 4947–4949 (2012).
19. X. Lin, N. Nilius, H.-J. Freund, M. Walter, P. Frondelius, K. Honkala, H. Häkkinen, Quantum well states in two-dimensional gold clusters on MgO thin films. *Phys. Rev. Lett.* **102**, 206801 (2009).
20. Q. Zhou, S. Kaappa, S. Malola, H. Lu, D. Guan, Y. Li, H. Wang, Z. Xie, Z. Ma, H. Häkkinen, N. Zheng, X. Yang, L. Zheng, Real-space imaging with pattern recognition of a ligand-protected Ag<sub>374</sub> nanocluster at sub-molecular resolution. *Nat. Commun.* **9**, 2948 (2018).
21. Z. Li, H.-Y. T. Chen, K. Schouteden, T. Picot, K. Houben, T.-W. Liao, C. Van Haesendonck, G. Pacchioni, P. Lievens, E. Janssens, Size-dependent penetration of gold nanoclusters through a defect-free, nonporous NaCl membrane. *Nano Lett.* **16**, 3063–3070 (2016).
22. Z. Li, H.-Y. T. Chen, K. Schouteden, T. Picot, A. Hillion, G. Pacchioni, C. Van Haesendonck, E. Janssens, P. Lievens, Size-dependent dissociation of small cobalt clusters on ultrathin NaCl films. *Nano Res.* **10**, 1832–1839 (2017).
23. Z. Li, K. Schouteden, V. Iancu, E. Janssens, P. Lievens, C. Van Haesendonck, J. I. Cerdá, Chemically modified STM tips for atomic-resolution imaging of ultrathin NaCl films. *Nano Res.* **8**, 2223–2230 (2015).
24. H. Mönig, Copper-oxide tip functionalization for submolecular atomic force microscopy. *Chem. Commun.* **54**, 9874–9888 (2018).
25. D. Porath, Y. Levi, M. Tarabiah, O. Millo, Tunneling spectroscopy of isolated C<sub>60</sub> molecules in the presence of charging effects. *Phys. Rev. B* **56**, 9829–9833 (1997).
26. J. Wang, G. Wang, J. Zhao, Structures and electronic properties of Cu<sub>20</sub>, Ag<sub>20</sub>, and Au<sub>20</sub> clusters with density functional method. *Chem. Phys. Lett.* **380**, 716–720 (2003).
27. E. M. Fernández, J. M. Soler, I. L. Garzón, L. C. Balbás, Trends in the structure and bonding of noble metal clusters. *Phys. Rev. B* **70**, 165403 (2004).
28. K.-J. Hu, S. R. Plant, P. R. Ellis, C. M. Brown, P. T. Bishop, R. E. Palmer, Atomic resolution observation of a size-dependent change in the ripening modes of mass-selected Au nanoclusters involved in CO oxidation. *J. Am. Chem. Soc.* **137**, 15161–15168 (2015).

29. K. J. Taylor, C. L. Pettiette-Hall, O. Cheshnovsky, R. E. Smalley, Ultraviolet photoelectron spectra of coinage metal clusters. *J. Chem. Phys.* **96**, 3319–3329 (1992).
30. D.-e. Jiang, M. Walter, Au<sub>40</sub>: A large tetrahedral magic cluster. *Phys. Rev. B* **84**, 193402 (2011).
31. W. Huang, M. Ji, C.-D. Dong, X. Gu, L.-M. Wang, X. G. Gong, L.-S. Wang, Relativistic effects and the unique low-symmetry structures of gold nanoclusters. *ACS Nano* **2**, 897–904 (2008).
32. H. Haberland, M. Mall, M. Moseler, Y. Qiang, T. Reiners, Y. Thurner, Filling of micron-sized contact holes with copper by energetic cluster impact. *J. Vac. Sci. Technol. A* **12**, 2925–2930 (1994).
33. K. Schouteden, K. Lauwaet, E. Janssens, G. Barcaro, A. Fortunelli, C. Van Haesendonck, P. Lievens, Probing the atomic structure of metallic nanoclusters with the tip of a scanning tunneling microscope. *Nanoscale* **6**, 2170–2176 (2014).
34. I. Horcas, R. Fernández, J. M. Gómez-Rodríguez, J. Colchero, J. Gómez-Herrero, A. M. Baro, WSxM: A software for scanning probe microscopy and a tool for nanotechnology. *Rev. Sci. Instrum.* **78**, 013705–013708 (2007).
35. J. P. Perdew, K. Burke, M. Ernzerhof, Generalized gradient approximation made simple. *Phys. Rev. Lett.* **77**, 3865–3868 (1996).
36. G. Kresse, J. Hafner, Ab initio molecular dynamics for liquid metals. *Phys. Rev. B* **47**, 558–561 (1993).
37. G. Kresse, J. Furthmüller, Efficient iterative schemes for ab initio total-energy calculations using a plane-wave basis set. *Phys. Rev. B* **54**, 11169–11186 (1996).
38. P. E. Blöchl, Projector augmented-wave method. *Phys. Rev. B* **50**, 17953–17979 (1994).
39. K. Lauwaet, K. Schouteden, E. Janssens, C. Van Haesendonck, P. Lievens, M. I. Trioni, L. Giordano, G. Pacchioni, Resolving all atoms of an alkali halide via nanomodulation of the thin NaCl film surface using the Au(111) reconstruction. *Phys. Rev. B* **85**, 245440 (2012).
40. Z. Li, H.-Y. T. Chen, K. Schouteden, K. Lauwaet, L. Giordano, M. I. Trioni, E. Janssens, V. Iancu, C. Van Haesendonck, P. Lievens, G. Pacchioni, Self-doping of ultrathin insulating films by transition metal atoms. *Phys. Rev. Lett.* **112**, 026102 (2014).
41. S. Grimme, Semiempirical GGA-type density functional constructed with a long-range dispersion correction. *J. Comput. Chem.* **27**, 1787–1799 (2006).
42. M. C. Robinson, A. C. H. Hallett, The static dielectric constant of NaCl, KCl, and KBr at temperatures between 4.2 °K and 300 °K. *Can. J. Phys.* **44**, 2211–2230 (1966).

#### Acknowledgments

**Funding:** This research was supported by the National Natural Science Foundation of China (11704057), the starting funding from HIT Shenzhen (HA45001082), and the KU Leuven Research Council (project GOA/14/007). Z.L., K.S., and T.P. acknowledge support from the Research Foundation Flanders (FWO) for a postdoctoral grant. Z.L. acknowledges the Research Network WOG-W003016N of the FWO for a short-term visit to KU Leuven. H.-Y.T.C. acknowledges financial support provided by Ministry of Science and Technology, Taiwan (MOST 106-2112-M-007-001-MY3) and the computing resource of TAIWANIA in National Center for High-Performance Computing (NCHC), Taiwan. The work of G.P. is supported by the Italian MIUR through the PRIN project 2015K7FZLH. **Author contributions:** Z.L., T.P., E.J., and P.L. designed the study. Z.L. and K.S. performed STM measurements. Z.L. and T.P. analyzed the data. H.-Y.T.C. and G.P. conducted DFT calculations. Z.L., T.P., T.-W.L., and A.S. deposited Au<sub>20</sub> clusters. C.V.H., E.J., and P.L. directed the research project. Z.L. wrote the first version of the manuscript. All authors discussed the results and participated in writing the manuscript. **Competing interests:** The authors declare that they have no competing interests. **Data and materials availability:** All data needed to evaluate the conclusions in the paper are present in the paper and/or the Supplementary Materials. Additional data related to this paper may be requested from the authors.

Submitted 18 June 2019

Accepted 7 November 2019

Published 3 January 2020

10.1126/sciadv.aay4289

**Citation:** Z. Li, H.-Y. T. Chen, K. Schouteden, T. Picot, T.-W. Liao, A. Seliverstov, C. Van Haesendonck, G. Pacchioni, E. Janssens, P. Lievens, Unraveling the atomic structure, ripening behavior, and electronic structure of supported Au<sub>20</sub> clusters. *Sci. Adv.* **6**, eaay4289 (2020).